Analysis of characteristics of a diode-pumped rubidium vapour laser using a kinetic algorithm

He Cai, You Wang, Wei Zhang, Liangping Xue, Hongyuan Wang, Juhong Han, Guofei An, Zhigang Jiang, Ming Gao, Jie Zhou, Zhiye Liao

Abstract. **We consider diode-pumped alkali vapour lasers (DPALs), which make it possible to achieve a high output power. Characteristics of such DPALs strongly depend on the physical properties of buffer gases and on structural parameters of a vapour cell. Special attention is paid to a diode-pumped rubidium vapour laser (DPRVL): We have investigated the effect of different conditions on its characteristics. The results show that the linewidth of the D$_2$ line of a DPRVL and the fine-structure mixing rate between two excited energy levels, which are two crucial factors in implementing a high-power DPRVL, increase with the pressure of buffer gases and the temperature of the vapour cell. It is demonstrated that the population ratio of two excited energy levels is close to that corresponding to a thermal equilibrium as the pressure of buffer gases and the temperature of the vapour cell become higher. We have found that the optimal values of the methane pressure, the cell temperature and the cell length can be determined through a kinetic analysis. The conclusions can be valuable for designing configurations of an end-pumped DPAL.**

Keywords: DPAL, DPRVL, buffer gas, vapour cell, linewidth, fine-structure mixing rate, number density, thermal equilibrium.

1. Introduction

The concept of a diode pumped alkali vapour laser (DPAL) was first proposed by Krupke in 2003 [1–3]. In recent years, DPALs have been rapidly developed because of their high Stokes efficiency, good beam quality, compact size and near-infrared emission wavelengths [4–12]. The Stokes efficiency of a DPAL can reach a miraculous level as high as 95.3% for caesium (Cs), 98.1% for rubidium (Rb) and 99.6% for potassium (K). The thermal effects in a DPAL are theoretically smaller than those of a conventional diode-pumped solid-state laser (DPSSL) [13, 14]. Additionally, the heat generated by a DPAL can be removed by circulating the gases inside an enclosed cavity [15, 16]. Therefore, the thermal management in a high-powered DPAL can be relatively simple. In fact, DPALs combine the advantages of both DPSSLs and conventional gas lasers; at the same time, they avoid their main disadvantages. It has been shown that a DPAL is now becoming one of the most promising candidates for simulta-

He Cai, You Wang, Wei Zhang, Liangping Xue, Hongyuan Wang, Juhong Han, Guofei An, Zhigang Jiang, Ming Gao, Jie Zhou, Zhiye Liao Southwest Institute of Technical Physics, Chengdu, Sichuan 610041, China; e-mail: youwang_2007@aliyun.com

neously achieving a good beam quality and a high output power [17, 18].

Among three normal types of DPALs, a diode-pumped rubidium vapour laser (DPRVL) has been recently drawing much attention [19–21]. A DPRVL is pumped on the D$_2$ transition, $5^2S_{1/2} \rightarrow 5^2P_{3/2}$, and generates on the D$_1$ transition, $5^2P_{1/2} \rightarrow 5^2S_{1/2}$ [5, 22, 23]. Although a DPRVL is somewhat similar to a common three-level DPSSL, some remarkable differences exist between them.

Generally, the local thermal equilibrium between the two upper-state levels can be easily maintained because of the fast relaxation rate for a conventional three-level DPSSL. For a DPRVL, the relaxation rate between the $^5P_{3/2}$ and $^5P_{1/2}$ levels is much slower than the stimulated transition rates [5]. The relaxation process between the $^5P_{3/2}$ level and the $^5P_{1/2}$ level is described by the fine-structure mixing rate for electrons of an alkali atom. The local thermal equilibrium between $^5P_{3/2}$ and $^5P_{1/2}$ levels is always untenable as the fine-structure mixing rate is small. Therefore, increasing the fine-structure mixing rate is essential in construction of a feasible DPAL by adding some kinds of buffer gases such as some hydrocarbons with small molecules, i.e. methane or ethane [24, 25].

Additionally, the pump transition linewidth of a DPRVL is much narrow (6.065 MHz) than that of a conventional DPSSL [5]. As a result, it is very hard to match such a narrow linewidth with the spectral width of a commercial diode pump laser (∼1000 GHz) [23, 26–28]. So, it is necessary to collisionally broaden the D$_2$ linewidth to ensure a high absorption with a rare gas such as helium [29]. Note that the buffer gases such as methane or ethane can also broaden the D$_2$ linewidth. To match the spectral width of high-power diodes, the pressure of rare gases must be increased to about several tens of atm [30, 31], which will make the designing and manufacturing a vapour cell rather challenging . With these limitations taken into account, narrowing of the pump linewidth becomes another feasible way to solve the problem.

After constructing a precise kinetic model, the factors that strongly affect the physical characteristic of a DPRVL should be carefully studied in detail. Among these factors, the cell temperature, the buffer gas pressure and the cell structure are thought to be the most important. The cell temperature produces a dominant influence on population of the number density in an alkali vapour cell [32]. In addition, the cell temperature and the pressure of buffer gases also determine both the fine-structure mixing rate and the broadened linewidth of the D$_2$ line. Among all structural parameters, the length of an alkali vapour cell is the most decisive because it is directly related to both the pump photon absorption rate and the laser photon emission rate. In this paper, we will discuss in detail the influence of three typical factors on the physical charac-

teristics of a DPRVL. To our knowledge, these problems have been scarcely studied in the literatures. We believe that our results will be helpful for designing and evaluating a DPAL.

Note also that as a high-gain three-level laser system, a DPRVL exhibits a high pump threshold. Actually, the quenching process reduces the population of the upper level spin–orbit states in a DPRVL [33, 34]. In this paper, quenching of the excited states has been taken account in the theoretical computation. It is worth pointing out that the kinetic process of quenching for a DPSSL is often neglected because of its extremely small value.

2. Kinetic model of a DPRVL

In this section, we will briefly describe the end-pumped kinetic model for a typical three-level DPRVL. The model is basically the same as in Ref. [5]. In the model, methane and helium are chosen as the buffer gases to mainly raise the fine-structure mixing rate and broaden the linewidth of the D_2 line, respectively. Note that quenching of the upper level spin–orbit states and the shift of the centre wavelength of the D_2 line, both arisen by two types of buffer gases, are considered in the calculation process.

Figure 1 shows electronic energy levels of rubidium atoms pumped, corresponding to D_1 and D_2 lines. In our study, all number densities of three levels are assumed constants inside the vapour cell in order to simplify the mathematical procedure. Thus, we can obtain the rate equations that determine the distribution of populations at the steady-state as follows:

$$\frac{dn_1}{dt} = 0 = -\Gamma_p + \Gamma_{las} + n_2(A_{21} + Q_{21}) + n_3(A_{31} + Q_{31}),$$

$$\frac{dn_2}{dt} = 0 = -\Gamma_{las} + \gamma_{32}\left[n_3 - 2n_2\exp\left(-\frac{\Delta E}{k_B T}\right)\right] - n_2(A_{21} + Q_{21}),$$

$$\frac{dn_3}{dt} = 0 = \Gamma_p - \gamma_{32}\left[n_3 - 2n_2\exp\left(-\frac{\Delta E}{k_B T}\right)\right] - n_3(A_{31} + Q_{31}),$$

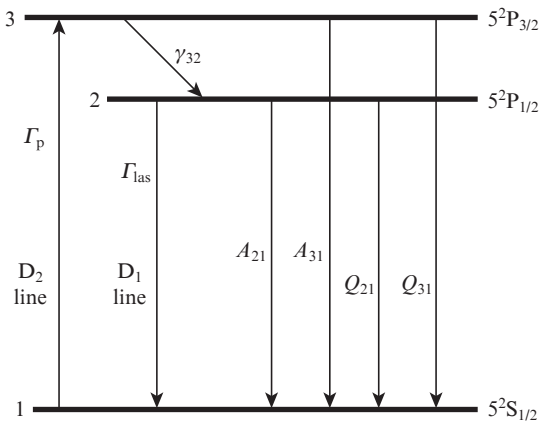$$n_0 = n_1 + n_2 + n_3,$$

(1)

Figure 1. Energy level diagram and main processes in the active medium of a DPRVL (Γ_p and Γ_{las} are the pump photon absorption rate and the laser photon emission rate, respectively; γ_{32} is the fine-structure mixing rate related to the relaxation rate from the $^2P_{3/2}$ level to the $^2P_{1/2}$ level; A and Q are the spontaneous emission rate and the quenching rate, respectively; n_1, n_2 and n_3 are, respectively, the alkali number densities at $^2S_{1/2}$, $^2P_{1/2}$ and $^2P_{3/2}$ levels).

where ΔE is the energy gap between the $^2P_{1/2}$ and $^2P_{3/2}$ levels k_B is the Boltzman constant; T is the cell temperature in Kelvin; and

$$n_0 = \frac{133.322}{k_B T} \times 10^{2.881 + 4.312 - \frac{4040}{T}}$$

(2)

is the total alkali number density in the cell, which is generally expressed as a function of the cell temperature [35].

The fine-structure mixing rate increases by adding such buffer gases as methane and helium; it is expressed as

$$\gamma_{32} = n_{met} V_r^{Rb-met} \sigma_{met} + n_{He} V_r^{Rb-He} \sigma_{He},$$

(3)

where n_{met} and n_{He} are the number densities of methane and helium inside the cell, respectively;

$$V_r^{Rb-met} = \sqrt{3k_B T\left(\frac{1}{m_{Rb}} + \frac{1}{m_{met}}\right)},$$

$$V_r^{Rb-He} = \sqrt{3k_B T\left(\frac{1}{m_{Rb}} + \frac{1}{m_{He}}\right)}$$

(4)

are, respectively, the rms thermally averaged relative velocities between rubidium atoms and methane molecules and helium atoms; m_{Rb}, m_{He} and m_{met} are the masses of a rubidium atom, a helium atom and a methane molecule, respectively; and σ_{met} and σ_{He} are the fine-structure mixing cross sections of methane and helium, respectively. In the calculation, both σ_{met} and σ_{He} were assumed constant at different temperatures.

The quenching rate by the buffer gases in the cell has the form

$$Q_{31} = n_{met} V_r^{Rb-met} \sigma_q^{met} + n_{He} V_r^{Rb-He} \sigma_q^{He},$$

(5)

where σ_q^{met} and σ_q^{He} are the quenching cross sections corresponding to methane and helium, respectively. The computation of Q_{21} is similar to Q_{31}.

For a typical end-pumped laser with a double-pass pump configuration shown in Fig. 2, Γ_P and Γ_{las} can be expressed by [5]:

$$\Gamma_p = \frac{\eta_{mode}\eta_{del}}{V_{las}} \int \frac{\lambda}{hc} P_p(\lambda)\left\{1 - \exp\left[-\left(n_1 - \frac{n_3}{2}\right)\sigma_{D_2}(\lambda)l\right]\right\}$$

$$\times \left\{1 + R_p\exp\left[-\left(n_1 - \frac{n_3}{2}\right)\sigma_{D_2}(\lambda)l\right]\right\}d\lambda,$$

$$\Gamma_{las} = \frac{P_{las}R_{oc}}{V_{las}h\nu_{las}(1 - R_{oc})}\left(\frac{1}{\sqrt{T_{tr}^2 R_{oc}}} - 1\right)(1 + \sqrt{T_{tr}^2/R_{oc}}),$$
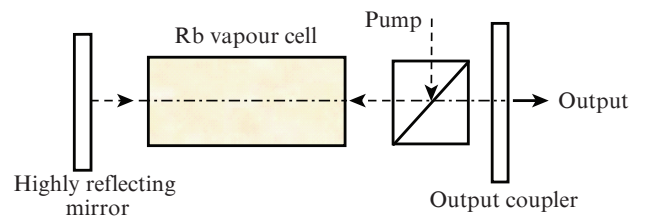
(6)

Figure 2. Schematic diagram for an end pumped DPRVL with a double-pass pump configuration.

where η_{mode} is the mode match efficiency for a DPRVL and a diode laser; η_{del} is the pump delivery efficiency from the pump source to the laser medium; V_{las} is the mode volume of the alkali laser (often assumed to be the fundamental mode); l is the cell length; $P_{\mathrm{p}}(\lambda)$ is the spectrally resolved pump power with a Gaussian distribution profile; P_{las} is the output alkali laser power; T_{tr} is the one-way cavity transmittance; R_{p} is the reflectance of the pump light at a highly reflecting mirror in the laser cavity; and R_{oc} is the reflectance of the output coupler. In the model, we consider the homogeneous collisional broadening of the D_2 line to be much greater than the inhomogeneous Doppler broadening due to the existence of helium and methane buffer gases. Therefore, the spectrally resolved pump absorption cross section $\sigma_{\mathrm{D}_2}(\lambda)$ can be approximately expressed by

$$\sigma_{\mathrm{D}_2}(\lambda) = \sigma_{\mathrm{D}_2}^0 \left[1 + \left(\frac{(\lambda - \lambda_{\mathrm{D}_2})2c}{\Delta\nu_{\mathrm{D}_2}\lambda^2}\right)^2\right]^{-1}, \tag{7}$$

where $\Delta\nu_{\mathrm{D}_2}$ is the pump absorption linewidth (FWHM) broadened by the buffer gases; and λ_{D_2} is the centre wavelength of the D_2 line, which shifts with the partial pressure of buffer gases. The parameters in (7) are determined by the formulae [36]:

$$\Delta\nu_{\mathrm{D}_2} = \Gamma_{\mathrm{D}_2}^{\mathrm{He}} P_{\mathrm{He}} \sqrt{T/353} + \Gamma_{\mathrm{D}_2}^{\mathrm{met}} P_{\mathrm{met}} \sqrt{T/393},$$

$$\sigma_{\mathrm{D}_2}^0 = \frac{\Delta\nu_{\mathrm{D}_2}^{\mathrm{rad}}}{\Delta\nu_{\mathrm{D}_2}} \sigma_{\mathrm{D}_2}^{\mathrm{rad}}, \tag{8}$$

$$\lambda_{\mathrm{D}_2} = \lambda_{\mathrm{D}_2}^{\mathrm{vac}} + \delta_{\mathrm{He}} P_{\mathrm{He}} + \delta_{\mathrm{met}} P_{\mathrm{met}},$$

where $\Gamma_{\mathrm{D}_2}^{\mathrm{He}}$ and $\Gamma_{\mathrm{D}_2}^{\mathrm{met}}$ are, respectively, the broadening coefficients of the D_2 line related to helium and methane (they were measured at 353 and 393 K, respectively, [39,40]); δ_{He} and δ_{met} are the line shifting coefficients of the D_2 line for helium and methane; P_{He} and P_{met} are the partial pressures of helium and methane in the cell; $\Delta\nu_{\mathrm{D}_2}^{\mathrm{rad}}$ is the natural linewidth of the D_2 line; $\sigma_{\mathrm{D}_2}^{\mathrm{rad}}$ is the atomic cross section of rubidium; and $\lambda_{\mathrm{D}_2}^{\mathrm{vac}}$ is the wavelength of the D_2 line in vacuum.

Additionally, the following relationship must be satisfied while the alkali laser maintains a steady output:

$$\exp[2(n_2 - n_1)\sigma_{\mathrm{D}_1}^0 l]T_{\mathrm{tr}}^2 R_{\mathrm{oc}} = 1, \tag{9}$$

where $\sigma_{\mathrm{D}_1}^0$ is the broadened cross section of the D_1 line, which can be computed by using the procedure similar to that for calculation of $\sigma_{\mathrm{D}_2}^0$.

In inspecting Eqns (1)–(9), it is obvious that the output characteristics of a DPRVL are related to the cell temperature and the pressure of buffer gases. The flowchart for computing the output power is shown in Fig. 3. The main parameters used in the evaluation process are listed in Table 1. In the calculations, we used MatLab programmes and the results obtained are considered in the next section.

3. Results and discussions

In this section, we investigate the influence of different physical conditions on the characteristics of a DPRVL. The results are calculated by using the kinetic model introduced above. The temperature is assumed to be uniform along the cell direction and the gradient between the cell wall and the gases is neglected in the calculation.

Table 1. Main parameters used in the theoretical simulation.

| Parameter	Value	Reference
A_{21}	3.61×10^7 s^{-1}	[5]
A_{31}	3.81×10^7 s^{-1}	[5]
$\sigma_{\mathrm{q}}^{\mathrm{He}}$	3×10^{-20} cm^2	[37]
$\sigma_{\mathrm{q}}^{\mathrm{met}}$	1.90×10^{-18} cm^2	[34]
ΔE	4.71×10^{-21} J	[5]
η_{mode}	0.92	
η_{del}	0.90	
R_{p}	0.99	
R_{oc}	0.20	
T_{tr}	0.85	
σ_{met}	4.20×10^{-15} cm^2	[38]
σ_{He}	1.84×10^{-17} cm^2	[37]
$\Gamma_{\mathrm{D}_1}^{\mathrm{He}}$	18.00 MHz Torr^{-1}	[39]
$\Gamma_{\mathrm{D}_2}^{\mathrm{He}}$	18.10 MHz Torr^{-1}	[39]
$\Gamma_{\mathrm{D}_1}^{\mathrm{met}}$	29.10 MHz Torr^{-1}	[40]
$\Gamma_{\mathrm{D}_2}^{\mathrm{met}}$	26.20 MHz Torr^{-1}	[40]
δ_{He}	0.37 MHz Torr^{-1}	[40]
δ_{met}	−7.00 MHz Torr^{-1}	[40]
$\sigma_{\mathrm{D}_1}^{\mathrm{rad}}$	1.08×10^{-9} cm^2	[35]
$\sigma_{\mathrm{D}_2}^{\mathrm{rad}}$	1.94×10^{-9} cm^2	[35]
$\lambda_{\mathrm{D}_1}^{\mathrm{vac}}$	780.2 nm	[35]
$\lambda_{\mathrm{D}_2}^{\mathrm{vac}}$	795 nm	[35]
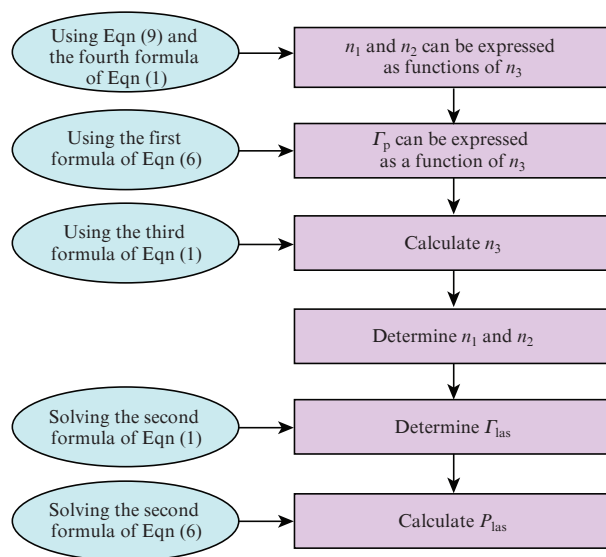
Figure 3. Flowchart for calculation of the output power.

3.1. Influences of buffer gases on the broadened linewidth of the D_2 line

As mentioned above, it is essential to broaden the linewidth of the D_2 line of rubidium atoms to match the linewidth of a pump laser-diode module. Generally, the collisionally broadened linewidth is physically determined by the features of buffer gases and the cell temperature. The broadened linewidth of helium and methane at different cell temperatures is shown in Fig. 4. One can see that increasing the pressure of buffer gases can efficiently broaden the linewidth of the D_2 line, with methane being a little more efficient than helium. However, it is necessary to point out that an even higher pressure of methane might bring about some disadvantages, e.g. the laser
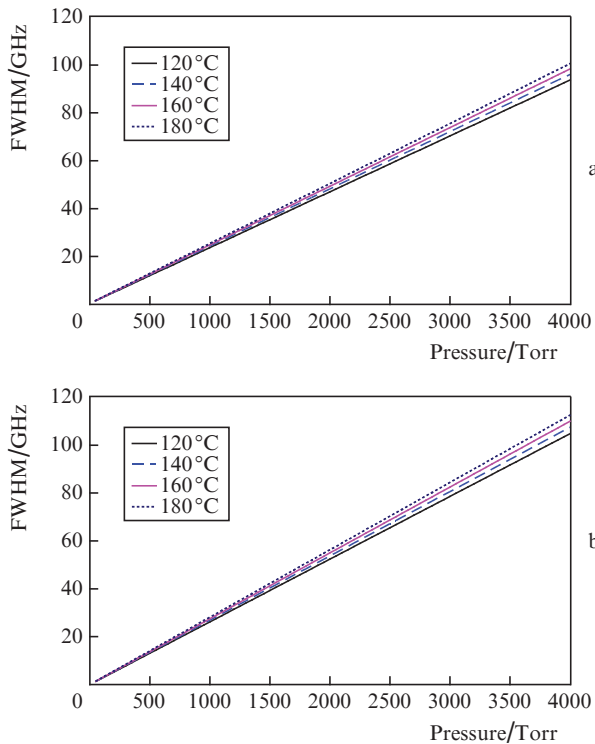
Figure 4. Dependences of the collisionally broadened FWHM of the D_2 line of rubidium on the pressure of (a) helium and (b) methane at different cell temperatures.

Figure 5. Fine-structure mixing rates as functions of (a) the cell temperature and (b) pressure for several kinds of buffer gases.

snow and the carbon deposit on the inner tube wall [41]. Additionally, when the pressure of buffer gases is maintained unchanged, the linewidth broadening can also be improved by raising the cell temperature.

It is worth noting that the process of the linewidth broadening will also narrow the cross section of the D_2 line, which will decrease the pump absorption rate for a DPRVL. One can consequently deduce that there should be an optimal pressure of the buffer gas to achieve a maximum laser output. In designing a feasible DPAL, adding too much buffer gas is not always a wise choice.

3.2. Fine-structure mixing rate under different conditions

The fine-structure mixing rate describes the relaxation rates between the $^2P_{3/2}$ level and the $^2P_{1/2}$ level. Figure 5 shows the fine-structure mixing rate as a function of the cell temperature and the gas pressure for three kinds of hydrocarbons with small molecules. One can see that the fine-structure mixing rate increases by adding buffer gases such as ethane, methane and ethane. It is obvious that raising the pressure of buffer gases in a DPRVL is a more effective way for increasing the fine-structure mixing rate. Although ethane is the most suitable among three types of buffer gases, we only concentrate on methane in this study because methane is thought to have the smallest carbon depositions on the cell walls.

To observe how the fine-structure mixing rate influences the output power, we employ the imaginary values of fine-structure mixing rate in the calculation. All the parameters used in the simulation are the same as those of methane, except for the fine-structure mixing rate. Figure 6 presents the output power of a DPRVL changing with the imaginary 'fine-
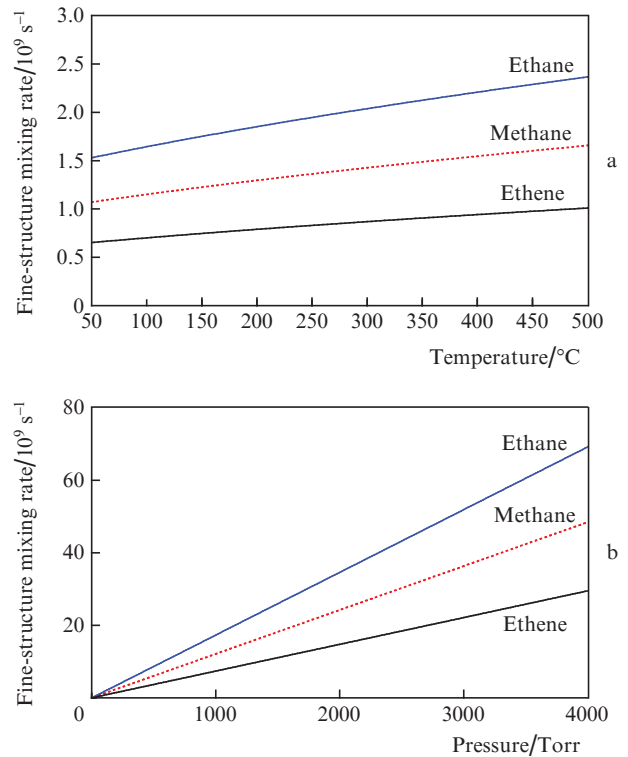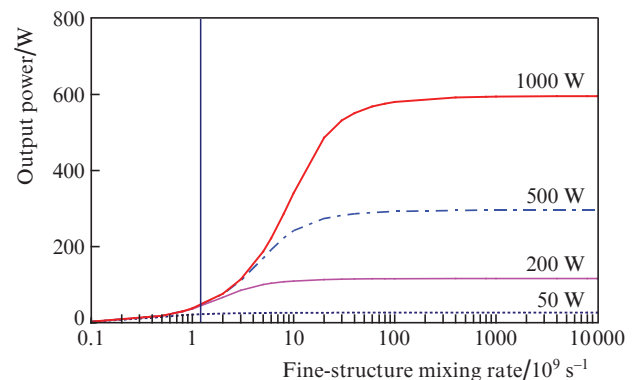

Figure 6. Output power as a function of the imaginary fine-structure mixing rate for different pump powers. The real fine-structure mixing rate for $P_{met} = 100$ Torr is 1.21×10^9 s^{-1}.

structure mixing rate' for different pump powers. During the evaluation, the cell length was 4 cm, the cell temperature was 140 °C, and the pressures of helium and methane were 100 and 500 Torr, respectively.

One can see from Fig. 6 that the output power of a DPRVL can be remarkably increased when the fine-structure mixing rate is smaller than a certain value for different pump powers. When the imaginary fine-structure mixing rate exceeds such a value, the laser power will keep to a steady saturation state. It is seen that choosing a buffer gas with a much faster fine-structure mixing rate is crucial for a higher pump power. The reason can be as follows: the population of $^2P_{3/2}$ level is required to relax more quickly for obtaining a higher output power especially for the high-pump case.

3.3. Populations at three energy levels under different conditions

To examine the dynamic features of a DPRVL, it is necessary to investigate how the populations at every energy level change with changing the buffer gas pressure and the cell temperature. Note that the data in all the figures are obtained by assuming the laser output to be constant.

Effect of methane pressure. In Figs 7a–7c, the number densities n_1, n_2 and n_3 are expressed as functions of the pressure of methane at different pump intensities. In the calculations, the cell temperature was set equal to 140 °C, the pressure of helium was 500 Torr, and the cell length was 4 cm.

One can see from Figs 7a–7c that n_1 first increases and then decreases slightly with increasing methane pressure. In turn, n_2 increases with the pressure of methane and n_3 shows a roughly opposite trend. These phenomena can be explained as follows. When the pressure of methane increases, the fine-structure mixing rate becomes faster and more populations are quickly relaxed from the $^5P_{3/2}$ level to the $^5P_{1/2}$ level, i.e. n_2 becomes larger. On the other hand, $\sigma_{D_1}^0$ decreases with increasing pressure of methane. It follows from Eqn (9) that the variation of n_1 is a synthetical result corresponding to an increase in n_2 and a decease in $\sigma_{D_1}^0$. When the methane pressure is lower than a certain value, the effect of the increase in n_2 is much more prevailing than that of the decrease in $\sigma_{D_1}^0$, and n_1 exhibits a tendency to enhancement. When the methane pressure exceeds such a value, the decrease in $\sigma_{D_1}^0$ becomes the mainstream and n_1 exhibits a diminishing tendency.

From Figs 7a–7c it is also seen that n_1 and n_2 become smaller with increasing pump power, whereas n_3 exhibits an opposite tendency, i.e., the population distribution can also be affected by the pump power except for the methane pressure. It follows from Eqn (6) that the higher the pump power, the greater the pump absorption rate, which implies more populations will transit from the $^5S_{1/2}$ level to the $^5P_{3/2}$ level.

Using the evaluated number densities of three energy levels, we can compare the ratio of n_3/n_2 for a real DPRVL with that corresponding to the local thermal equilibrium (Fig. 7d). While the methane pressure increases, the curves for a real DPRVL tend towards that of the thermal equilibrium due to the higher fine-structure mixing rate. In addition, the smaller the pump power, the closer the curves to that of the thermal equilibrium state. This occurs mainly because the pump absorption rate is relatively slow for weak pump radiation while the fine-structure mixing rate remains almost unchanged.

Effect of cell temperature. Figures 8a–8c show how the cell temperature affects the population densities n_1, n_2 and n_3 under different pump conditions. In the calculations, the cell length was 4 cm, and the pressures of methane and helium were 100 and 500 Torr, respectively. It is obvious that n_1, n_2 and n_3 greatly increase with the cell temperature, because the total number density n_0 in the alkali-vapour cell rapidly increases at an even higher cell temperature.

Dependences of the ratio n_3/n_2 on the cell temperature at different pump powers of a real DPRVL are shown in Fig. 8d. For comparison, an assumed curve under the local thermal equilibrium condition is also drawn in the figure. When the
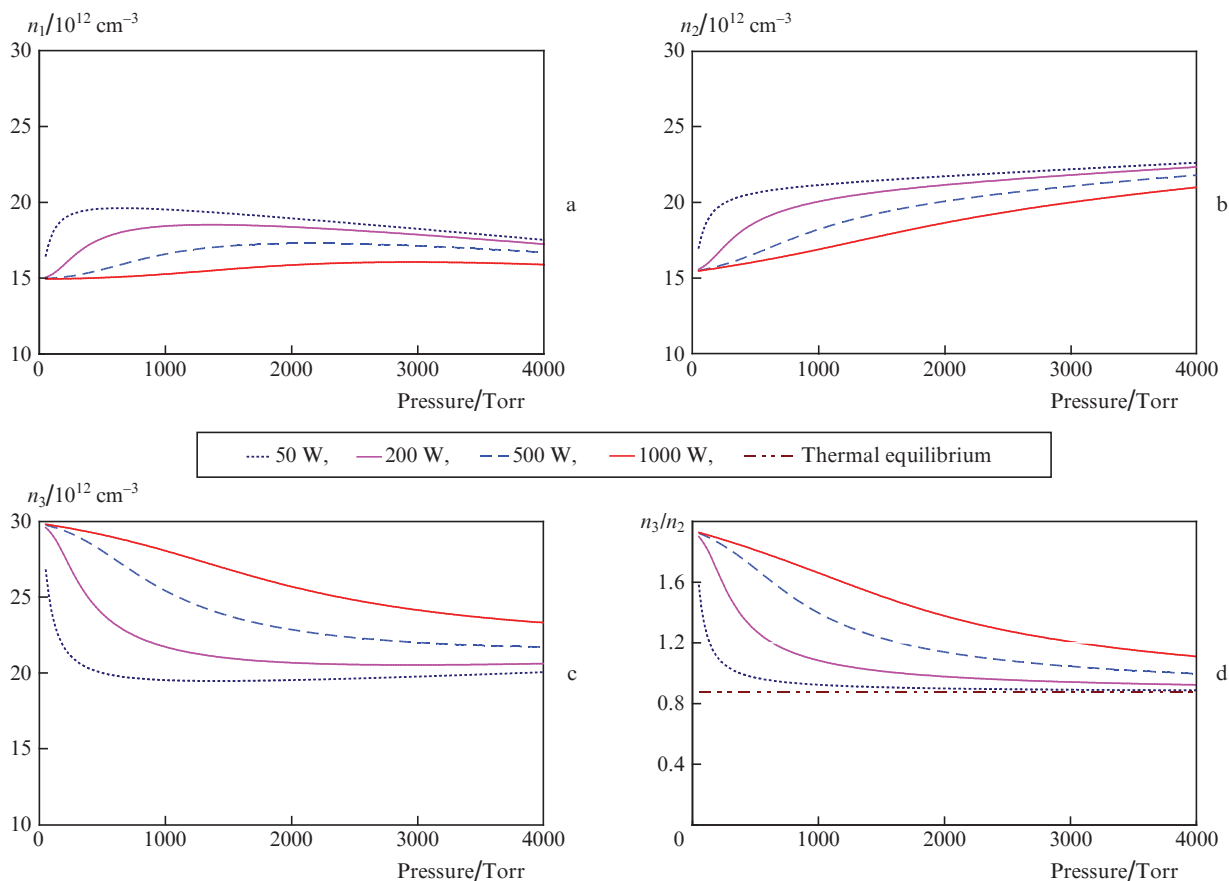

Figure 7. Dependences of (a) n_1, (b) n_2 and (c) n_3 on the methane pressure; (d) the ratios n_3/n_2 at pump powers of 50, 200, 500 and 1000 W.
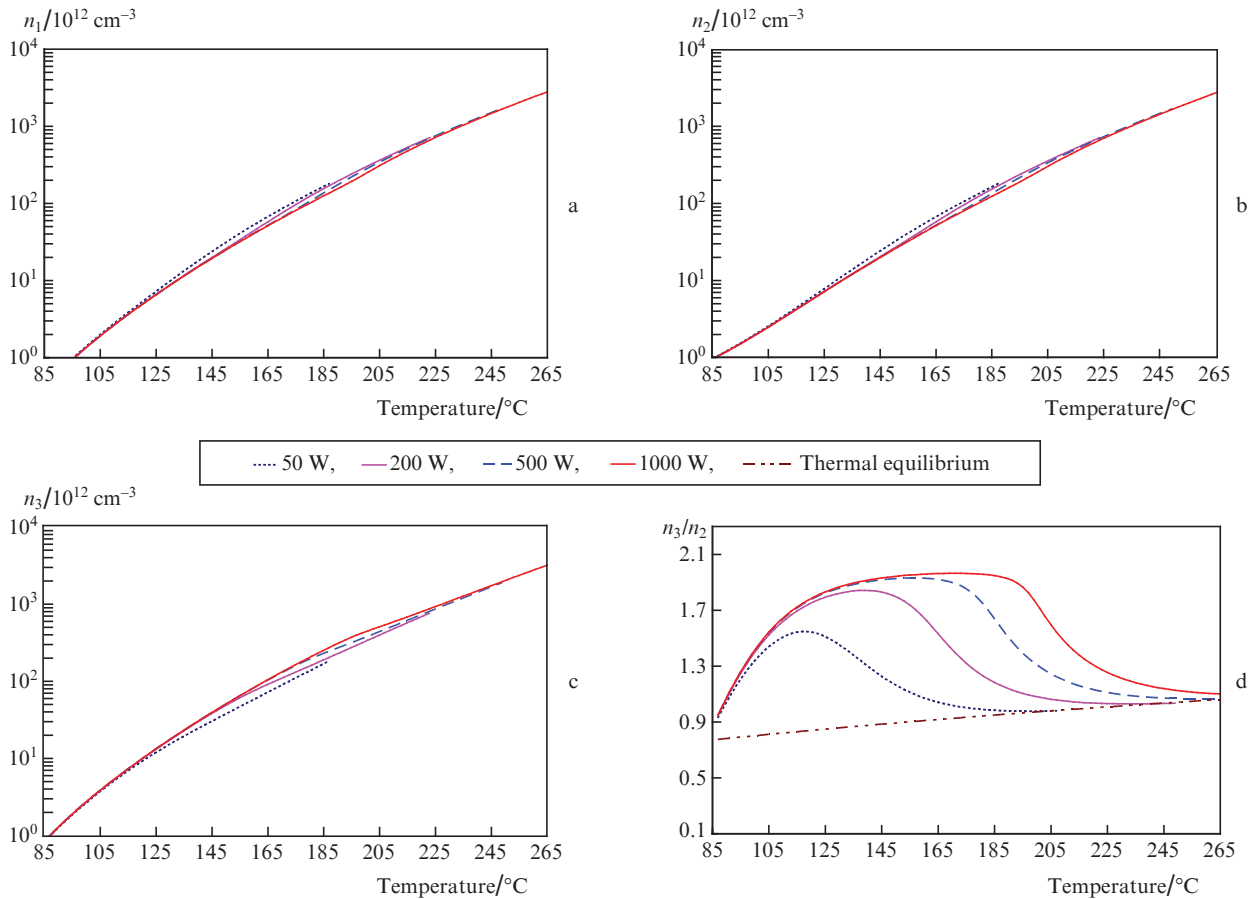
Figure 8. Dependences of (a) n_1, (b) n_2 and (c) n_3 on the cell temperature; (d) the ratios n_3/n_2 at pump powers of 50, 200, 500 and 1000 W.

cell temperature increases, the curves for a real DPRVL first become far away from that of the thermal equilibrium and then approach the thermal equilibrium state. We can also see from Fig. 8d that the ratios n_3/n_2 roughly decrease with decreasing pump power. Note that the closer these ratio to the ratio under the thermal equilibrium, the less stable the laser state, i.e., accessing the thermal equilibrium state is not always an advisable selection to obtain a high output from a DPRVL.

3.4. Output laser power under different conditions

By utilising the above-obtained values of n_1, n_2 and n_3, the output power of a DPRVL can be evaluated by using an algorithm schematically illustrated in Fig. 3. Here, we examine the conditions determining the output characteristics of the laser.

Effect of cell temperature. As analysed in Section 2, the number densities (and the total number density n_0 of the rubidium vapour) are largely dependent on the cell temperature. Naturally, the output power of a DPRVL will be strongly governed by the same parameter. As shown in Fig. 9, it is obvious that the output power of a DPRVL first increases until reaching a maximum value and then falls as the cell temperature rises. As above, in the calculations, the cell length was 4 cm, and the pressures of helium and methane were 500 and 100 Torr, respectively.

The reason for the existence of the optimum cell temperature can be explained as follows. The transition rate of pump photon absorption Γ_p first increases with the cell temperature
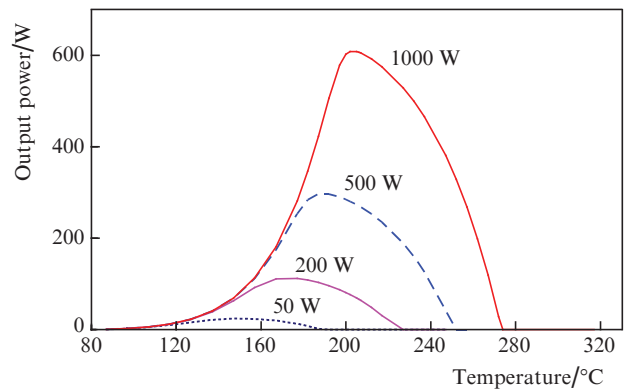

Figure 9. Output power of the laser as a function of the cell temperature for pump powers of 50, 200, 500 and 1000 W.

and then reaches a saturation status (Fig. 10). One can deduce that when the cell temperature is low, the number density of alkali atoms is small enough to maintain a sufficient transition rate of the pump photon absorption Γ_p and the laser power is therefore small. On the other hand, if the cell temperature becomes too high, n_2 and n_3 increase to a level several orders higher than that of a low temperature (see Figs 8a–8c). It follows from the first formula of Eqn (1) that Γ_{las}, which is proportional to the output power, will decrease in this case, while Γ_p will remain almost unchanged. It means that raising the cell temperature is not always a correct way to obtain a
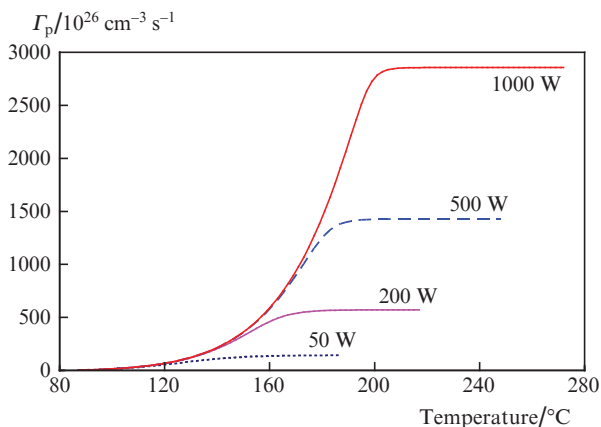
Figure 10. Pump photon absorption rate vs. cell temperature at different pump powers.

high power of a DPRVL. We can also conclude that the output power is sensitive to the cell temperature especially for a higher pump intensity.

Effect of methane pressure. Figure 11 shows the influence of the methane pressure on the laser output power under different pump conditions. The data were obtained for the cell temperature of 140 °C and the cell length of 4 cm. It is clear that there are also optimum conditions for obtaining a maximum output power. When the methane pressure becomes higher, the fine-structure mixing rate increases and the cross section of the D_2 line decreases. Such two contrary ways simultaneously dominate the output characteristics in Fig. 11. Therefore, an extremely high methane pressure will also not lead to a high output power at a fixed cell temperature.
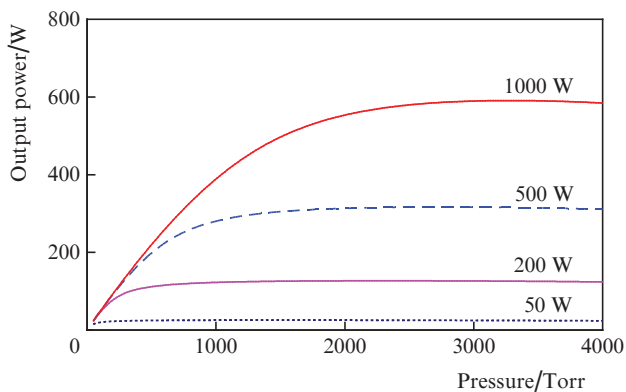

Figure 11. Output power of the laser as a function of methane pressure at pump powers of 50, 200, 500 and 1000 W.

Effect of cell length. In Fig. 12, the output power of the laser is shown as a function of the cell length at different cell temperatures. In the calculations, the pump power was 50 W, the helium pressure was 500 Torr, and the methane pressure was 100 Torr. It is easy to notice that as the cell length increases, the output power first raises and then begins to fall after reaching a maximum value, because the pump absorption rate Γ_p has the relationship with both the media length and the volume of the laser mode. These two parameters provide two opposite tendencies to Γ_p [see Eqn (6)]. Dependences in Fig. 12 give the optimal cell length, which can be helpful in

designing a real DPRVL. Note that although the optimum cell length varies at different cell temperatures, the output power of the laser corresponding to an optimum cell length is almost the same for all cases. The results demonstrate that lengthening of the cell will not always result in an increase in the output of a DPRVL if the pump power is kept constant.
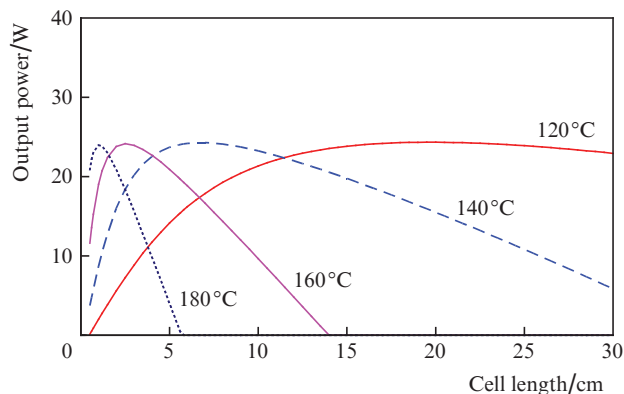

Figure 12. Output power of the laser as a function of cell length at cell temperatures of 120, 140, 160 and 180 °C.

Figure 13 shows the output power of the laser as a function of the cell length at different pump powers. In the calculations, the cell temperature was 140 °C. The pressures of helium and methane were the same as those in Fig. 12. One can see that an increase in the cell length leads to an increase in the output power if the cell temperature is invariable. It follows from Figs 12 and 13 that the experimental conditions must be considered together when determining an adequate cell length.
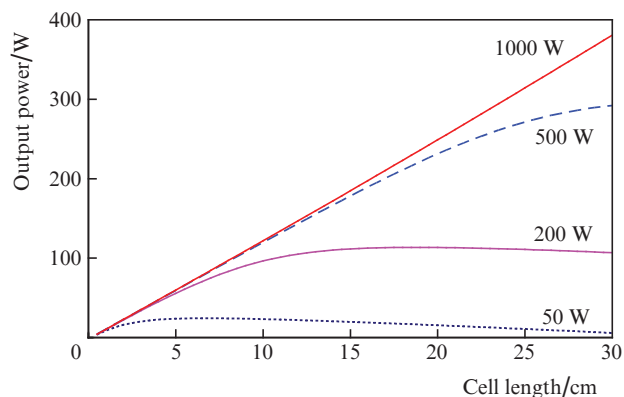

Figure 13. Output power of the laser as a function of cell length at various pump intensities.

4. Conclusions

In this paper, some main characteristics of an end-pumped DRPVL, including the broadened linewidth of the D_2 line, the fine-structure mixing rate, the population distribution of three energy levels and the laser output power, are analysed by employing a kinetic model. Both the quenching process of the upper levels and the shift of the centre wavelength of

the D_2 line have been taken into account in the calculations. The result shows the cell temperature and the pressure of the buffer gases greatly affect the physical features of a DPRVL. The population ratio n_3/n_2 of two excited energy levels in a steady state is closer to that of the thermal equilibrium with an even higher methane pressure or an even higher cell temperature. We have also demonstrated that there are the optimal values of the methane pressure, cell temperature and cell length, which is important for the design of an efficient DPRVL.

It is worth noting that some assumptions have been used in the simulation. Both the cell temperature and the alkali atom density have been assumed constants inside the media cell. The effects of the temperature on the fine-structure mixing cross section and the pump absorption cross section have been ignored in construction of the theoretical model. All these assumptions would undoubtedly bring about some analytic deviations. A further analysis will be undertaken in our future research.

References

1. Krupke W.F., Beach R.J., Kanz V.K., Payne S.A. *Opt. Lett.*, **28** 2336 (2003).
2. Krupke W.F. US Patent Application US 2003/0099272 A1 (2003).
3. Krupke W.F., Beach R.J., Payne S.A., Kanz V.K., Early J.T. *AIP Conf. Proc.*, **702**, 367 (2004).
4. Beach R.J., Krupke W.F., Kanz V.K., Payne S.A., Dubinskii M.A., Merkle L.D., in *Advanced Solid-State Photonics (TOPS)*. Ed. by G. Quarles (Optical Society of America, Optics and Photonics, 2004) Vol. 94, paper 479.
5. Beach R.J., Krupke W.F., Kanz V.K., Payne S.A. *J. Opt. Soc. Am. B*, **21**, 2151 (2004).
6. Page R.H., Beach R.J., Kanz V.K. *Opt. Lett.*, **31**, 353 (2006).
7. Wang Y., Kasamatsu T., Zheng Y., Miyajima H., Fukuoka H., Matsuoka S., Niigaki M., Kubomura H., Hiruma T., Kan H. *Appl. Phys. Lett.*, **88**, 141112 (2006).
8. Zhdanov B.V., Knize R.J. *Opt. Lett.*, **32**, 2167 (2007).
9. Wang Y., Niigaki M., Fukuoka H., Zheng Y., Miyajima H., Matsuoka S., Kubomura H., Hiruma T., Kan H. *Phys. Lett. A*, **360**, 659 (2007).
10. Sulham C.V., Perram G.P., Wilkinson M.P., Hostutler D.A. *Opt. Commun.*, **283**, 4328 (2010).
11. Yang Z.N., Wang H.Y., Lu Q.S., Hua W.H., Xu X.J. *Opt. Lett.*, **19**, 23118 (2011).
12. Liu Y.F., Pan B.L., Yang J., Wang Y.J., Li M.H. *IEEE J. Quantum Electron.*, **48**, 485 (2012).
13. Zhdanov B. et al. *Opt. Commun.*, **270**, 353 (2007).
14. Zweiback J., Komashko A. *Proc. SPIE Int. Soc. Opt. Eng.*, **7915**, 791509 (2011).
15. Yang Z.N., Wang H.Y., Lu Q.S., Li Y.D., Hua W.H., Xu X.J., Chen J.B. *J. Opt. Soc. Am. B*, **28**, 1353 (2011).
16. Barmashenko B.D., Rosenwaks S. *Opt. Express*, **37**, 3615 (2012).
17. Komashko A., Zweiback J. *Proc. SPIE Int. Soc. Opt. Eng.*, **7581**, 75810H (2010).
18. Bogachev A.V., Garanin S.G., Dudov A.M., et al. *Kvantovaya Elektron.*, **42**, 95 (2012) [*Quantum Electron.*, **42**, 95 (2012)].
19. Gourevitch A., Venus G., Smirnov V., Glebov L. *Opt. Lett.*, **32**, 2611 (2007).
20. Zhdanov B.V., Stooke A., Boyadjian G., Voci A., Knize R.J. *Opt. Lett.*, **33**, 414 (2008).
21. Miller W.S., Sulham C.V., Holtgrave J.C., Perram G.P. *Appl. Phys. B*, **103**, 819 (2011).
22. Pitz A., Perram P. *Proc. SPIE Int. Soc. Opt. Eng.*, **7005**, 700526 (2008).
23. Hager G.D., Perram G.P. *Appl. Phys. B*, **101**, 45 (2010).
24. Krupke W.F. *Progr. Quantum Electron.*, **36**, 4 (2012).
25. Zhdanov B.V., Knize R.J. *Opt. Eng.*, **52**, 021010 (2013).
26. Zhdanov B.V., Stooke A., Boyadjian G., Voci A., Knize R.J. *Opt. Express*, **16**, 748 (2008).
27. Zhdanov B.V., Sell J., Knize R.J. *Electron. Lett.*, **44**, 582 (2008).
28. Yang Z.N., Li Y.D., Wang H.Y., Lu Q.S., Xu X.J. *Chin. Opt. Lett.*, **9**, 061401 (2011).
29. Zhu Q., Pan B.L., Chen L., Wang Y.J., Zhang X.Y. *Opt. Commun.*, **283**, 2406 (2010).
30. Wu S.S.Q., Soules T.F., Page R.H., Mitchell S.C., Kanz V.K., Beach R.J. *Opt. Lett.*, **32**, 2423 (2007).
31. Zweiback J., Krupke W.F. *Opt. Express*, **18**, 1444 (2010).
32. Rice C.A., Lott G.E., Perram G.P. *Appl. Opt.*, **51**, 8102 (2012).
33. Hostutler D.A., Hager G.D., Heaven M.C. *Proc. SPIE Int. Soc. Opt. Eng.*, **7005**, 700522 (2008).
34. Zameroski N.D. et al. *J. Phys. B: At. Mol. Opt. Phys.*, **42**, 1 (2009).
35. Steck D.A. http://steck.us/alkalidata
36. Yang Z.N., Wang H.Y., Lu Q.S., Liu L., Li Y.D., Hua W.H., Xu X.J., Chen J.B. *J. Phys. B: At. Mol. Opt. Phys.*, **44**, 085401 (2011).
37. Sell J.F., Gearba M.A., Patterson B.M., Byrne D., Jemo G., Lilly T.C., Meeter R., Knize R.J. *J. Phys. B: At. Mol. Opt. Phys.*, **45**, 055202 (2012).
38. Hrycyshyn E.S., Krause L. *Can. J. Phys.*, **48**, 2761 (1970).
39. Romalis M.V., Miron E., Gates G.D. *Phys. Rev. A*, **56**, 4569 (1997).
40. Rotondaro M.D., Perram G.P. *J. Quant. Spectrosc. Radiat. Transfer*, **57**, 497 (1997).
41. Zhdanov B.V., Knize R.J. *Electron. Lett.*, **43**, 1024 (2007).